Appl. Phys. B 71, 711–716 (2000) / Digital Object Identifier (DOI) 10.1007/s003400000425

Applied Physics B
Lasers
and Optics

Flame growth and wrinkling in a turbulent flow

C.F. Kaminski[1], X.S. Bai[2], J. Hult[1], A. Dreizler[3], S. Lindenmaier[3], L. Fuchs[2]

[1] Division of Combustion Physics, Lund Institute of Technology, 22100 Lund, Sweden
(Fax: +46-46/2229858, E-mail: clemens.kaminski@forbrf.lth.se)
[2] Division of Fluid Dynamics, Lund Institute of Technology, 22100 Lund, Sweden
[3] Institut für Technische Verbrennung, Pfaffenwaldring 12, 70569 Stuttgart, Germany

Received: 12 April 2000/Revised version: 26 June 2000/Published online: 5 October 2000 –

Abstract. High-speed planar laser-induced fluorescence (PLIF) and 3-D large eddy simulations (LES) are used to study turbulent flame kernel growth, wrinkling and the formation of separated flame pockets in methane/air mixtures. Turbulence was effected by a set of rotary fans situated in a cylindrical enclosure. Flame wrinkling was followed on sequential 2-D OH images captured at kHz repetition rates. Under stoichiometric conditions and low turbulence levels the flame kernel remains singly connected and close to spherical in shape. By increasing turbulence or reducing the stoichiometry of the mixture the formation of separated pockets could be observed and studied. The mechanisms behind these phenomena are investigated qualitatively by LES of a level-set G-equation describing the flame surface propagation in turbulent flows.

PACS: 47.27.-i; 42.62.-b

Although flame-turbulence interactions are of fundamental interest to combustion science [1] the phenomenon still poses a severe challenge to theorists and experimentalists alike because of the time-dependent and three-dimensional nature of the problem [2]. Turbulent eddies can wrinkle the flame and even quench it; on the other hand, eddies improve heat transfer and the mixing of species which increase the efficiency of technical combustion devices.

Much of the present understanding on this topic stems from the study of simple and isolated flame vortex interactions (FVI) in laminar flames. Mostly two-dimensional vortices were studied exhibiting rotational motion. Because of the simple geometry of this problem and the controlability of the vortex, this situation is ideally suited for investigation and has indeed provided fundamental and important new insights. For example, both experimental [3–7] and theoretical [8, 9] FVI studies have confirmed that the domain of the laminar flamelet regime is much larger than suggested by the Klimov–Williams criterion on the Borghi diagram. Ashurst and McMurtry [10] confirmed that the vortex strength may be increased by the flame from FVI studies. Microelectrostatic probe measurements of FVI [11] have shown that the scale of flame wrinkling is much larger than the Kolmogorov scale, consistent with the earlier hypothesis that it is mostly large eddies that wrinkle the flame [12].

For practical turbulent combustion situations these FVI studies are far too idealized systems since here the problem is always three-dimensional in nature and characterized by a large number of length- and time-scales. Vortex motion is random and includes translational as well as rotational components.

The objective of the present work was to study flame-eddy interactions in a more realistic three-dimensional flame situation, using both advanced laser diagnostic imaging techniques and three-dimensional large eddy simulation (LES). The object of study was the growth of a premixed flame kernel subjected to controlled degrees of turbulence. Methane air mixtures were subjected to turbulence in a specially designed ignition cell [13] in which four high-speed fans were incorporated. The growth of the flame kernel in this system can be characterized by three phases: an initially laminar kernel moving in a turbulent flow field; subsequent growth with increasing degrees of flame wrinkling; and finally the development to a fully turbulent flame structure. In a related paper, flame *initiation* by the spark discharge in the cell was investigated both experimentally and theoretically [14]. In [14] high-speed spectroscopic imaging data was compared to a full direct numerical simulation (DNS) in two dimensions including detailed chemistry. At this early stage the chemistry is very complex (because of the high temperature peak and gradients during the discharge) although the flame remains small and its topology rather simple (laminar-like). At a later stage the situation becomes too complex and three-dimensional in nature to allow such an approach. Here, we present the results using a three-dimensional large eddy simulation (LES) into which chemistry is incorporated using the flamelet-G concept [12, 15]. The LES framework allows us to address not only the turbulent regime, but also the earlier transitional phase. We start the calculation es-

This paper is dedicated to Professor Dr. Jürgen Wolfrum on the occasion of his 60th birthday.

sentially at a time point where the spark-ignition event is over and a self-sustaining, (initially) laminar flame kernel has been established. The calculations are qualitatively compared to temporal sequences of the flame topology obtained by ultrahigh-speed planar laser-induced fluorescence imaging (PLIF) of the OH radical. It should be pointed out that direct comparisons of sequential instantaneous data are meaningful only in a qualitative sense because of the chaotic behavior of turbulence.

1 Experimental setup

The laser source of the high-speed OH PLIF system is a Nd:YAG laser cluster consisting of four individual pulsed Nd:YAG lasers. Rapid bursts of four laser pulses were obtained by firing the individual lasers in series. The excitation wavelength for OH was obtained by frequency doubling a dye laser pumped by the output of the Nd:YAG laser cluster. A high-speed camera based on eight intensified CCD cameras was used to detect the OH PLIF signal. By exposing the individual CCD cameras sequentially, very fast image sequences can be captured. The details of the system are given elsewhere [13, 16, 17]. Briefly, OH was excited using the temperature insensitive $Q_1(8)$ transition in the $A\,^2\Sigma^+(v'=1) \leftarrow X\,^2\Pi(v''=0)$ electronic band near 283 nm with subsequent detection occurring primarily in the (1,1) and (1,0) vibronic bands around 309 nm. The experiments were carried out in a completely characterized turbulent ignition cell [13, 14]. It incorporated a highly sophisticated ignition system providing very reproducible ignition events with precisely determined energy doses. Controlled amounts of turbulence could be introduced via four high-speed rotating fans incorporated into the cell (a schematic drawing of the geometry is given in Fig. 1, which is not drawn to scale). The PLIF imaged region covered a volume of $2\times2\times2\times10^{-2}\,\mathrm{cm}^3$.

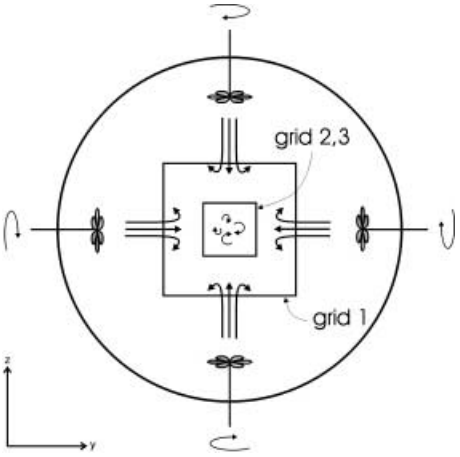

Fig. 1. Sketch of the geometry of the ignition cell and the three computational domains employed in the calculations. Grids 1, 2, and 3 are three cubic domains with successively increasing numerical resolutions: Grid 1: $10^3\,\mathrm{cm}^3$ with 50^3 mesh points; grid 2: $3^3\,\mathrm{cm}^3$ with 50^3 mesh points; and grid 3: $6^3\,\mathrm{cm}^3$ with 98^3 mesh points. Shear-flow-generated turbulence is established in the middle of the cell by four opposing fans. Ignition occurs in the center of the domains. The x axis is in a direction perpendicular to the plane of the drawing

2 Theory

In LES the continuity equation and Navier–Stokes equations are spatially filtered. The interaction between the smallest resolved eddies and the unresolved eddies is taken into account by a sub-grid-scale (SGS) term in the governing equations for which a model has to be used in order to close the system of equations. In the past, various SGS models have been proposed. One of the simplest models is the Smagorinsky model [18], which is based on the assumption that the SGS stresses are proportional to the velocity gradient of the resolved scales multiplied by a positive scalar, the so-called eddy viscosity. It can be shown that models based on the eddy viscosity always transfer energy from the large resolved scales to the small unresolved scales but are unable to account for energy transfer from small to resolved scales (backscatter). Other models, such as similarity models [19] and dynamic models [20], have been proposed in the literature to deal with this backscattering problem. Here we employ a stress similarity model originally proposed by Liu et al. [19].

The flame front propagation is calculated using a level-set G-equation approach. The G-equation is derived from a kinematic balance between the flow velocity and the burning velocity [12, 15, 21]. The flame front is defined to be the surface (level) corresponding to $\overline{G}=0$; on the other hand, $\overline{G}<0$ and $\overline{G}>0$ represents the unburned and post-flame zones, respectively. In the LES context, the space-filtered level-set G-equation has the form

$$\frac{\partial\overline{G}}{\partial t}+\widetilde{u}_j\frac{\partial\overline{G}}{\partial x_j}=\left[S_\mathrm{L}^0+u''-S_\mathrm{L}^0\mathcal{L}\kappa(\overline{G})+\mathcal{L}K(\overline{G})\right]\left|\frac{\partial\overline{G}}{\partial x_j}\right|, \quad (1)$$

where S_L^0 is the unstretched laminar flame speed, which depends on the initial temperature, pressure and fuel/air ratio of the mixture. $\mathcal{L}$ is the Markstein length, which indicates how strongly the flame curvature and strain influence the flame burning velocity. For large-scale and low-intensity turbulent flows, Clavin and Williams [22] suggested that, for unity Lewis number mixtures

$$\frac{\mathcal{L}}{l_\mathrm{F}}=\frac{1}{\gamma}\ln\frac{1}{1-\gamma}\quad\gamma=\frac{T_\mathrm{b}-T_\mathrm{u}}{T_\mathrm{b}}, \quad (2)$$

where l_F is the unstretched laminar flame thickness; T_b is the postflame zone temperature and T_u is the unburned zone temperature. In (1), $\kappa(\overline{G})$ is the curvature of the resolved flame surface and $K(\overline{G})$ is the resolved flame strain rate. They are defined as

$$\kappa(\overline{G})=\nabla\cdot\boldsymbol{n},\quad K(\overline{G})=\boldsymbol{n}\cdot\nabla\widetilde{\boldsymbol{V}}\cdot\boldsymbol{n},\quad \boldsymbol{n}=-\nabla\overline{G}/\left|\nabla\overline{G}\right|, \quad (3)$$

where $\boldsymbol{n}$ is the normal vector to the flame surface towards the unburned mixture; $\widetilde{\boldsymbol{V}}$ is the resolved velocity vector with its component $\widetilde{u}_j$ in the x_j direction. The influence of the unresolved small scale tends to wrinkle the flame front which leads to an acceleration of the unburned fuel/air consumption speed. This effect is modeled in analogy to the Damköhler turbulent flame speed theory: one adds a characteristic sub-grid-scale fluctuation speed $u''=(u_j''u_j''/3)^{1/2}$ to the unstretched laminar burning velocity, as noted on the right-hand side of (1). By definition $u_j''=u_j-\widetilde{u}_j$, where u_j is the

exact velocity component, which is unknown in LES. Using the energy cascade model, one can argue that the dissipation rate is constant at different scales within the initial subrange (LES resolution scale) [23]. Therefore u'' is here modeled by

$$u'' = \left(\frac{\triangle_f}{\widehat{\triangle}_f}\right)^{1/3} \left[\frac{1}{3}\left(\widetilde{u}_j - \widehat{\widetilde{u}}_j\right)\left(\widetilde{u}_j - \widehat{\widetilde{u}}_j\right)\right]^{1/2}, \quad (4)$$

where $\widehat{\widetilde{u}}_j$ is the velocity component after applying a second Gaussian filter of width $\widehat{\triangle}_f$ on the LES resolved velocity component $\widetilde{u}_j$. The ratio of the first space filter width to the second filter width is $\triangle_f/\widehat{\triangle}_f = 2$.

In (1)–(4), the repetition of index j denotes summation over $j = 1, 2, 3$.

In the current LES, coupling of the level-set G-equation to the velocity field is simplified by neglecting the change of density associated with chemical heat release. This assumption has been employed in previous studies of flame structures and flame–vortex interactions [24] and in level-set simulations of the flame front [10, 25]. While it neglects the influence of heat release on the generation/destruction of turbulent vortices, the constant-density assumption does retain the effect of vortices acting on flame fronts, through the flame strain and curvature and SGS velocity fluctuations, as evidenced by (1). Future efforts will be directed at incorporating this aspect into the calculations.

The numerical calculation of the space-filtered continuity equation and momentum equations is performed on a uniformly distributed rectangular grid. The continuity equation is discretized using fourth-order central differences. The convection terms in the momentum equations are discretized using a third-order upwind scheme proposed in [26]. Other spatial terms in momentum equations are discretized using fourth-order central differences. The time integration is carried out using a three time-level second-order implicit scheme. As the turbulent flow studied here is at low Mach numbers, a Poisson equation for the pressure–velocity coupling is used. At each time step, a V-cycle multi-grid method is used to accelerate the iteration process. More details about the numerical scheme are found in [27]. The level-set (G-equation) is discretized using a third-order upwind scheme in space (similar to the scheme for the momentum equation) and explicit time marching, with CFL number 0.1. The G calculation is only performed within a narrow band around the zero level-set, with a bandwidth of six grid cells on each side of the zero level-set. Re-initialization of the G field to distance function is carried out by solving an equation of the type $|\nabla G| = 1$, using the numerical scheme suggested in [28].

3 Results

Figure 1 shows a schematic diagram of the experimental cell geometry, the flow configuration, and the computational domain. The x axis is assigned to be along the cylinder axis (perpendicular to the figure plane). The origin of the coordinate system is set at the geometrical center of the cell. OH PLIF images were taken in the $y-z$ plane near $x = 0$. The four fans in the figure were situated at a distance of 0.115 m from the cylinder axis. Computationally the cell was discretized using Cartesian grids. Three grid levels were used in the computation with successively increasing numerical resolution with 82^3 grid points for the first level in a 10^3-cm^3 domain. The second and third locally refined grids employ 50^3 and 98^3 mesh points in a 3^3-cm^3 domain (see Fig. 1). The small domain is about the same size as the measurement window. The mesh size in the third level grid is about 0.3 mm, smaller than the laminar flame thickness (see Table 2). At the boundaries of the first level grid a uniform inlet velocity profile (representing the four fans) is specified. The outlet profiles (representing boundary cells other than the inlets) are obtained by assigning zero normal gradients of the dependent variables. Boundary values on the second and third level grids are obtained by interpolations of the dependent variables from the first grid level. The solutions of the multi-level grid are conveniently obtained using the multi-grid solver [27].

To model in- and outflow conditions accurately and to properly account for recirculation and swirling motion the cylindrical vessel geometry should be taken into account. However, for the studies presented here, where we are interested in qualitative features of 3D-flame vortex interactions the simpler boundary conditions presented here are sufficient. In a quantitative comparison and statistical analysis of mean LES data with mean PLIF data a precise modeling of cell and rotor geometry is required in the fashion reported in [28].

Stoichiometric and lean mixtures were studied at two turbulence levels in the present work. The experimental conditions corresponding to the data presented in Figs. 2a, 3a and 4 are listed in Table 1. Parameters for corresponding LES calculations (Figs. 2b and 3b) are listed in Table 2.

Figure 2a shows a PLIF sequence of OH corresponding to a window size of about 2^2 cm^2 with a time difference of 1.7 ms between individual images. The images represent the flame boundary as marked by the OH radical concentration field. The OH boundary was obtained from the PLIF raw data by using the edge enhancement image processing algorithm delineated in [29]. The algorithm is based on anisotropic non-

Table 1. Flame conditions corresponding to Figs 2a, 3a, and 4. In the table ϕ denotes the fuel/air stoichiometric ratio, ω the fan speed, u' the turbulence intensity, τ_0 the delay of the first image from the spark, and $\Delta\tau$ the time separation between individual PLIF images. The change in flame speed with varying stoichiometry/turbulence conditions is clearly evident from the range of $\Delta\tau$ observed

Fig	ϕ	ω/rpm	u'/ms^{-1}	τ_0/ms	$\Delta\tau$/ms
2a	1	1000	0.62	1.50	1.7
3a	0.65	1000	0.62	2.50	3.0
4	1	3000	2.01	1.50	1.1

Table 2. List of numerical parameters used for the LES calculations presented in this paper

ϕ	S_L^0/m/s	δ_F/m	γ	$\mathcal{L}$/m	Δ_f/m	$S_L^0\mathcal{L}$/m^2
1.00	0.3915	5×10^{-4}	0.8666	1.1622×10^{-3}	1.8750×10^{-3}	4.5500×10^{-4}
0.65	0.1491	8×10^{-4}	0.8302	1.7086×10^{-3}	1.8750×10^{-3}	2.5475×10^{-4}

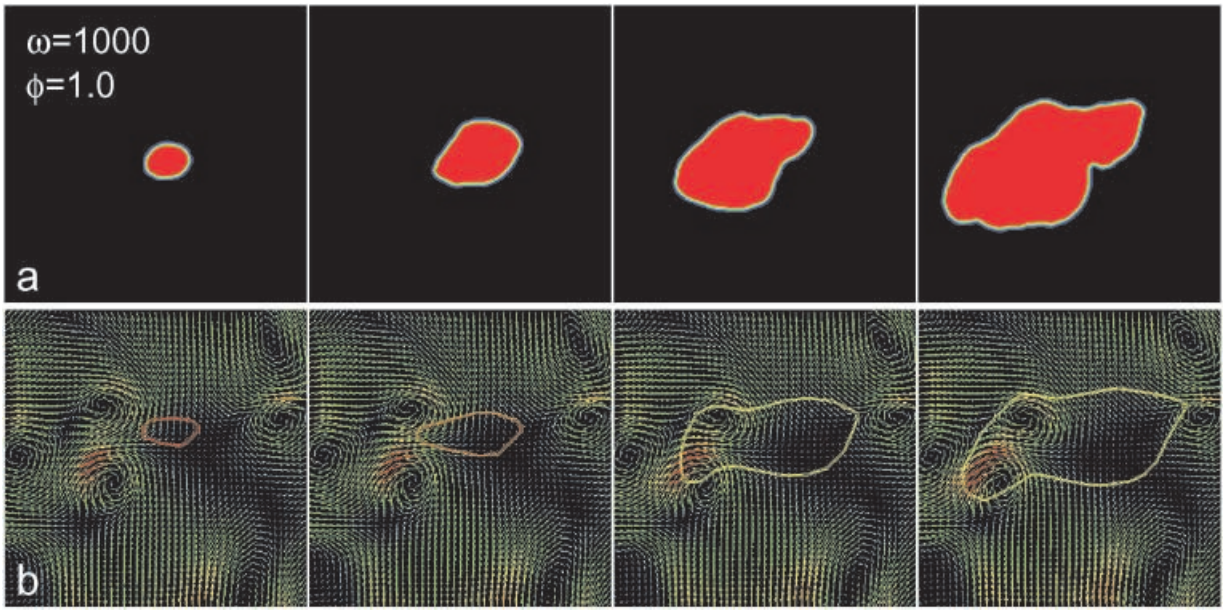

Fig. 2a,b. Evolution of the flame boundaries for a stoichiometric methane air mixture ($\phi = 1$) at low rotor speeds ($\omega = 1000$ rpm). **a** corresponds to experimental PLIF sequences obtained by imaging the OH radical. The conditions for the events shown are summarized in Table 1. **b** is the result of an LES run under similar conditions showing the calculated velocity field as well as the flame contour surface ($G = 0$ surface). The numerical parameters used for the calculation are listed in Table 2

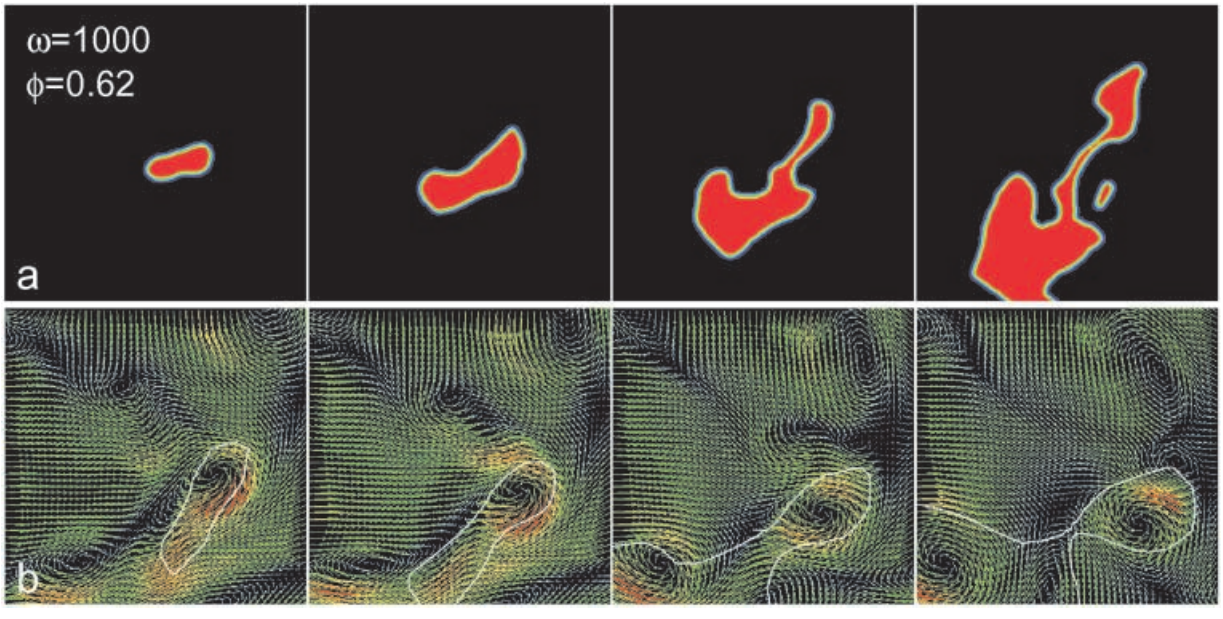

Fig. 3. a Evolution of flame boundaries for lean methane–air mixtures ($\phi = 0.62$ and $\omega = 1000$ rpm). In **b** the result from a corresponding LES run is shown. Conditions for the calculations are given in Table 2. The series shows the $G = 0$ flame surface superimposed on the velocity vector field

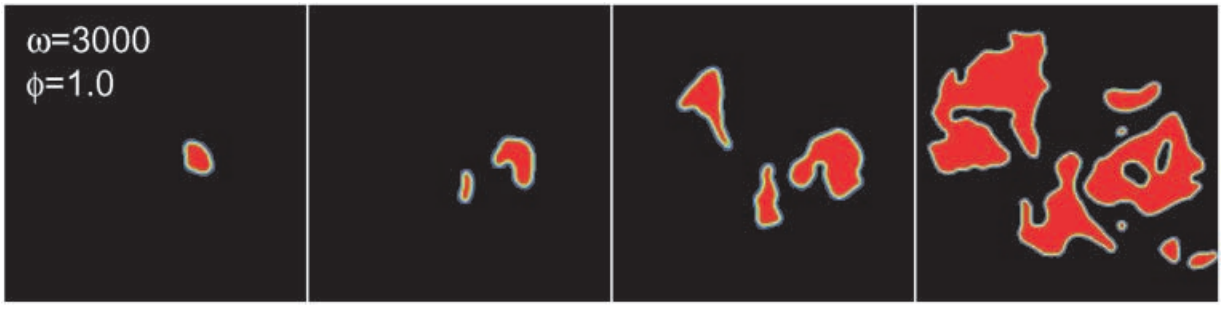

Fig. 4. Experimental flame profiles corresponding to the high-turbulence case studied ($\phi = 1$ and $\omega = 3000$ rpm)

linear diffusion filtering. The resulting edge-enhanced images were segmented into OH and non-OH areas with OH regions appearing red and non-OH regions black. Flame boundaries are highlighted in yellow.

The series clearly reveals the onset and increase of flame wrinkling with time. At these low levels of turbulence the stoichiometric flame (1000 rpm fan speed corresponding to turbulent rms fluctuations of $u' = 0.62\,\mathrm{ms}^{-1}$) remains almost spherical in shape and becomes only weakly wrinkled. The flame kernel remains singly connected and continuous as it grows. In Fig. 3a a PLIF sequence corresponding to a lean mixture ($\phi = 0.65$) is shown at the same turbulence level (1000 rpm). Clearly the flame exhibits a much stronger wrinkling with time than its stoichiometric counterpart in Fig. 2a. Even the likely formation of a pocket can be followed from the last two images in the series. Figure 4 corresponds to $\phi = 1$ at high turbulence levels (3000 rpm, $u' = 2.01\,\mathrm{ms}^{-1}$). Here the wrinkling is very strong from the beginning, flame pockets are formed very early in the sequence and the flame kernel becomes highly corrupted.

An important parameter that can be studied from the measured OH images is the turbulent flame burning speed. Even though it is difficult to evaluate the exact turbulent burning velocity (S_T) in this experiment, due to the present lack of simultaneous velocity data, one can easily notice the significant difference of S_T between Figs. 2a, 3a, and 4. The time interval between images for the stoichiometric 1000-rpm flame is 1.7 ms, compared to 1.1 ms for the 3000-rpm flame and 3 ms for the lean 1000-rpm flame (see Table 1 for conditions of the experiments presented here). This shows that the stoichiometric high-intensity turbulent flame burns much faster than the other two flames with the lean flame propagating slowest. This phenomenon has been the subject of numerous experimental and theoretical investigations [30]. For example, Damköhler suggested that $S_\mathrm{T} = S_\mathrm{L}(1 + u'/S_\mathrm{L})$, where S_L is the laminar burning velocity and u' is the speed of turbulent fluctuations. Note that S_L for the lean flame is lower than for the stoichiometric flame and u'/S_L is higher for the 3000-rpm flame which leads to the phenomena observed in the present case.

The 3-D LES calculations can be used to try to account for the observed differences in the wrinkling between lean and stoichiometric mixtures and for the phenomenon of flame pocket formation. The conditions for the simulations presented here are listed in Table 2. The unstretched laminar burning velocity S_L^0, the laminar flame thickness δ_F and the Markstein length $\mathcal{L}$ are calculated using a one-dimensional flame code [31] with the detailed chemical kinetic mechanism developed by Peters [32]. 30 species up to C3 are incorporated and 82 elementary reactions are employed. The flame thickness is defined here using the CH_2O profile and regions with CH_2O mole fractions less than 1% of their peak values were considered outside the flame zone.

In Fig. 2b the flame contour ($G = 0$) is displayed superimposed on the calculated velocity vector field. It can be seen how vortices produced by the fan-generated shear layers move around and interact with the flame front. Several vortices can be identified in the picture and one can clearly follow how they modify the flame kernel in time. The high-speed flow in the center of the dual-counter rotating vortices seen on the left-hand side of the diagram has the same direction as the flame kernel propagation, thus it tends to accelerate the kernel's growth and pulls it into the counter-rotating vortices. The flow streams in the outer wings of the vortex pair flow back towards the flame kernel. They thus act to resist the flame kernel propagation in these directions. The combination of these effects leads to the observed wrinkling of the flame front. In the last picture of the sequence one sees how the flame is being pulled into the right-hand vortex, thus stretching the kernel and making it oblong. Due to mass conservation unburned fuel and air flow towards the 'waist' of the flame kernel in between the 'pulling' vortices. The resulting strain leads to the oblong-shaped flame similar to the experimental data exhibited in Fig. 2a. It tends to resist the flame kernel growth radially out from the waist. In the stoichiometric case shown the effect of this is small, however if the SGS flame burning velocity ($S_\mathrm{L}^0 + u''$) is small (such as in the lean-flame case shown in Fig. 3a), the flame front can even be pushed back (similar to flame flash-back). If the flame kernel in between the vortices becomes too thin the middle of the flame kernel becomes separated, and two separated flame pockets are formed. This seems to be the process taking place in the lean mixture (Fig. 3). Local strain in the middle becomes so high that the flame becomes quenched there leading to pocket formation. This type of process seems to be evidenced in the experimental example (Fig. 3a) where a similar phenomenon can be observed. Note that the flame speeds and increased degree of wrinkling in the lean case are captured by the calculations. It is to be expected that if the intensity of turbulence is very high, vortex motion becomes more energetic, with much more violent effects on the flame kernel such as seen in Fig. 4.

Both flame curvature and strain have a significant influence on the formation of flame pockets. Strain in particular assists pocket formation which is also seen in the present study. In another numerical study and asymptotic analysis, Rogg and Peters [33, 34] showed that increasing strain leads to the decrease of the laminar burning velocity in methane/air mixtures. If the strain rate exceeds a critical value, the premixed flame front can be quenched. The phenomena illustrated in Fig. 3 are along this line. Note in particular, that the flame front in between the two vortex pairs in Fig. 2b and the 'flame-neck' shown in Fig. 3b, closely resemble the 'back-to-back' twin-flame studied by Rogg and Peters [33, 34]. The high strain rate acting on such flame fronts tends to decrease the laminar flame burning velocity, thus aiding the formation of multiple flame pockets.

4 Summary and conclusions

High-speed OH PLIF imaging has been used to measure flame kernel propagation, wrinkling and the formation of separated flame pockets in a fan-stirred cylindrical enclosure. Stoichiometric as well as lean methane/air mixtures subjected to different levels of turbulence have been studied and the observed phenomena have been investigated using 3D LES of the level-set G-equation including detailed chemistry.

With the measurement system employed the degree of flame wrinkling could be tracked in real time and its effect on turbulent flame velocities studied in a systematic manner. LES as reported here is well suited for comparisons with time-resolved measurement data as it helps an intuitive understanding of the underlying physics of observed phe-

nomena. The present approach reveals mechanisms by which lean flames can be destabilized even at relatively low turbulence intensities, conditions under which a stoichiometric flame is only moderately affected. Vortices in the turbulence field cause flame strain and curvature, ultimately leading to the onset of flame wrinkling and flame pocket formation. LES captures the wrinkling of the flame front by strong flow streams induced by vortex pairs. However since the structure of the vortices in the turbulence is very complex and three-dimensional, 2-D images may lead to false information about the flame pocket formation.

Current work is focusing on the simultaneous measurement of flow fields by particle imaging velocity (PIV) techniques [35, 36] in conjunction with the OH sequences. This will provide further details into the processes of flame–vortex interactions. In addition it represents a basis for even more direct and stringent validation of numerical studies. Future work will also focus on detailed statistical comparisons of results from the two approaches. For example a parametric investigation of flame kernel topology (surface-to-volume ratio, etc.) by the use of automated image post-processing routines [29] is envisaged.

Acknowledgements. One of the authors (CFK) would like to thank M. Aldén for helpful discussions and his continuous interest in this work. The LES work is partially supported by the Swedish natural science foundation (NFR) and the experimental work by the EU TMR programme 'Access to Large Scale Facilities', contract number ERBFMGECT950020 (DG12), which is gratefully acknowledged. JH acknowledges support by the Swedish Center for Combustion Science and Technology (CECOST).

References

1. F.A. Williams: *Combustion Theory*, 2nd edn. (Benjamin/Cummings 1985)
2. K.N.C. Bray: Proc. Combust. Inst. **26**, 1 (1996)
3. W.L. Roberts, J.F. Driscoll: Combust. Flame **87**, 245 (1991)
4. W.L. Roberts, J.F. Driscoll, M.C. Drake, L.P. Goss: Combust. Flame **94**, 58 (1993)
5. C.J. Mueller, J.F. Driscoll, D.L. Reuss, M.C. Drake, M.E. Rosalik: Combust. Flame **112**, 342 (1998)
6. V.R. Katta, C.D. Carter, G.J. Fiechtner, W.M. Rockmore, J.R. Gord, J.C. Rolon: Proc. Combust. Inst. **27**, 587 (1998)
7. H.N. Najm, P.H. Paul, C.J. Mueller, P.S. Wyckoff: Combust. Flame **113**, 312 (1998)
8. T. Poinsot, D. Veynante, S. Candel: J. Fluid Mech. **228**, 561 (1991)
9. T. Poinsot: Proc. Combust. Inst. **26**, 219 (1996)
10. W.M.T. Ashurst, P.A. McMurtry: Combust. Sci. Technol. **66**, 17 (1989)
11. J. Furukawa, K. Maruta, T. Hirano: Combust. Flame **112**, 293 (1998)
12. N. Peters: Four lectures on turbulent combustion. Lecture notes for ERCOFTAC Summer School, Sept. 15–19, 1997 (Aachen, 1997)
13. A. Dreizler, S. Lindenmaier, U. Maas, J. Hult, M. Aldén, C.F. Kaminski: Appl. Phys. B **70**, 287 (2000)
14. C.F. Kaminski, J. Hult, M. Aldén, S. Lindenmaier, A. Dreizler, U. Maas, M. Baum: Proc. Combust. Inst. **28**, (2000), in press
15. F.A. Williams: In *The Mathematics of Combustion*, ed. by J. Buckmaster, (SIAM, 1985) p. 97
16. C.F. Kaminski, J. Hult, M. Aldén: Appl. Phys. B **68**, 757 (1999)
17. T. Ding, T. van der Meer, M. Versluis, M. Golombok, J. Hult, M. Aldén, C.F. Kaminski: In Proc. of 3rd International Symposium on Turb., Heat, and Mass Trans. (Aichi Shuppan, Nagoya 2000) p. 857
18. J. Smagorinsky: Mon. Weath. Rev. **91**, 99 (1963)
19. S. Liu, C. Meneveau, J. Katz: J. Fluid Mech. **275**, 83 (1994)
20. M. Germano, U. Piomelli, P. Moin, W. Cabot: Phys. Fluids A **3**, 1790 (1991)
21. S. Osher, J.A. Sethian: J. Comput. Phys. **79**, 12 (1988)
22. P. Clavin, F.A. Williams: J. Fluid Mech. **116**, 251 (1982)
23. H. Tennekes, J.L. Lumley: *A First Course in Turbulence* (MIT Press, Cambridge, Mass 1972)
24. A.M. Leverdant, S.M. Candel: Combust. Sci. Tech. **60**, 79 (1988)
25. A. Kerstein, W.T. Ashurst, F.A. Williams: Phys. Rev. A **37**, 2728 (1988)
26. T. Kawamura, K. Kuwahara: AIAA paper 84-0340 (1984)
27. X.S. Bai, L. Fuchs, J. Gullbrand: AIAA Paper 97-0371 (1997)
28. M. Sussman, E. Fatemi, S. Osher: J. Comput. Phys. **114**, 146 (1994)
29. H. Malm, G. Sparr, J. Hult, C.F. Kaminski: J. Opt. Soc. Am. A, in press
30. D. Bradley: Proc. Combust. Inst. **24**, 247 (1992)
31. F. Mauss: Ph.D. Thesis, RWTH Aachen, 1998
32. N. Peters: In *Reduced Mechanisms for Applications in Combustion Systems: Lecture Notes in Physics*, ed by N. Peters, B. Rogg, **m-15**, (Springer, Berlin, Heidelberg 1993) p. 3
33. B. Rogg, N. Peters: Combust. Flame **79**, 402 (1990)
34. B. Rogg: Combust. Flame **73**, 45 (1988)
35. J.H. Frank, K.M. Lyons, M.B. Long: Combust. Flame **107**, 1 (1996)
36. J. Hult, G. Josefsson, M. Aldén, C.F. Kaminski: 10th International Symposium on Applications of Laser Techniques to Fluid Mechanics; (2000), Lisbon. Paper available under: http://in3.dem.ist.utl.pt/downloads/lxlaser2000/pdf/26_2.pdf